Chapter 5

Tetragonal CuO

Because of its relative simplicity, CuO is a candidate compound to study electron correlation effects and the influence of correlation on the electronic structure of transition metal compounds, in particular high temperature cuprate superconductors. In the cuprate superconductors the conductivity takes place in the copper oxide planes, which are sandwiched between charge reservoir layers. These planes have the composition CuO_2 and are arranged in a square pattern with the copper atoms on the corners and the oxygen atoms on the vertices between them. If another copper atom was placed in the middle of such a square a CuO rock salt plane would be created. If the charge reservoir layers were then removed and every second layer was given an offset of a Cu—O bond length, a three dimensional CuO rock salt structure would result, which would be a very interesting 3D potential model system with which to study the properties of high-T_c compounds.

There are, however, two problems: the proposed rock salt structure is not a stable phase of copper oxide, and the resulting structure would be a Mott insulator. To overcome these problems we have used epitaxial strain to force the CuO to grow in a tetragonal rock salt structure and studied the properties of this new tetragonal phase. The structural parameters were determined by using RHEED and x-ray photoemission diffraction. We had to resort to *in situ* measurement of the crystal structure because the films tended to relax to the more stable monoclinic CuO phase. Measuring properties was further complicated by the limited thickness (~2 nm) for which the tetragonal phase can be stabilized. Subsequently we studied the electronic structure with XPS and UPS. By comparing with stable copper oxides we have determined the Cu has a charge of +2 and that the tetragonal structure is more ionic than the monoclinic phase. To dope the material we have deposited overlayers to provide charge transfer to the CuO. Leaving aside the question of whether these electrons are localized or delocalized, we observe signs that the CuO is doped with electrons in this process. No Fermi edge was measured on these samples and when taken out of vacuum the alkali metals were found to have reacted with air, undoing any charge transfer effect. A UHV transfer chamber and a UHV, thin film scanning physical property measurement system are under development in our laboratory that will ameliorate such problems.

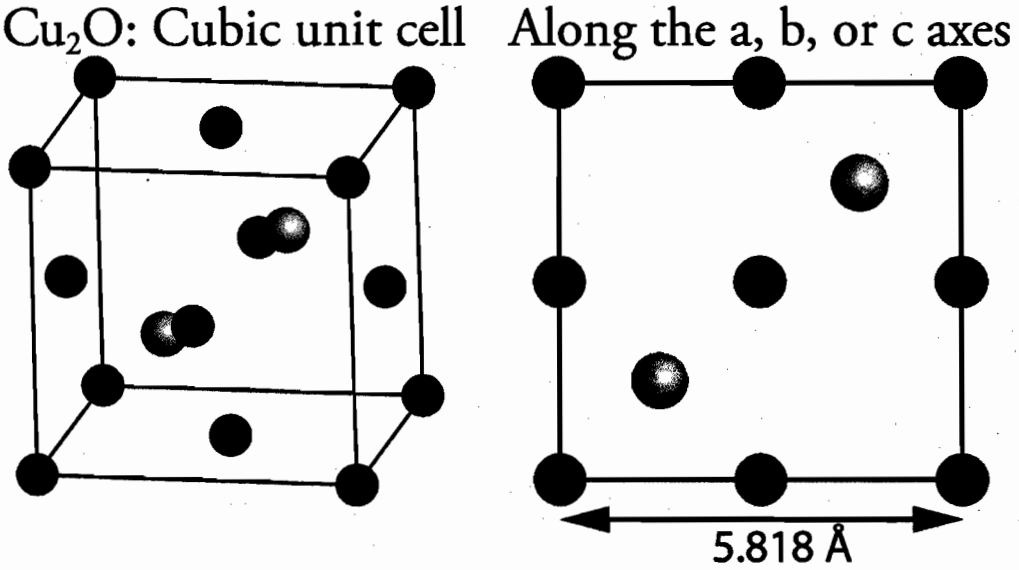

Figure 5.1: *An orthographic projection of the unit cell of cuprite (Cu_2O) is given on the left. The view along one of the crystal axes, together with the lattice parameter, is displayed on the right. Oxygen is represented by the larger lighter colored spheres and copper by the smaller darker colored spheres.*

This chapter describes these efforts and starts out with a general description of the well known stable oxides that can be formed with copper. The results of our experiments will be presented subsequently, followed by a discussion of the results and the conclusions.

5.1 The bulk oxides of copper

Copper can be progressively oxidized to form a number of oxides. It is important to know the properties of these oxides when a new phase is to be discerned. In this section the bulk structural, electronic, and magnetic properties of the natural oxides are summarized.

5.1.1 Structural properties

Copper metal has a face-centered-cubic (Fm-$3m$) lattice with a unit cell parameter of 3.604 Å,[1] which results in a Cu-Cu distance of 2.55 Å for nearest neighbors.

When copper is oxidized it first gives up one electron to become Cu^+ and forms Cu_2O, which is called cuprite and has space group Pn-$3m$. Cu_2O has a highly symmetric crystal structure: a cubic unit cell with a lattice parameter of 4.268 Å.[2] There are six atoms per unit cell; the oxygen atoms form a body-centered-cubic lattice and

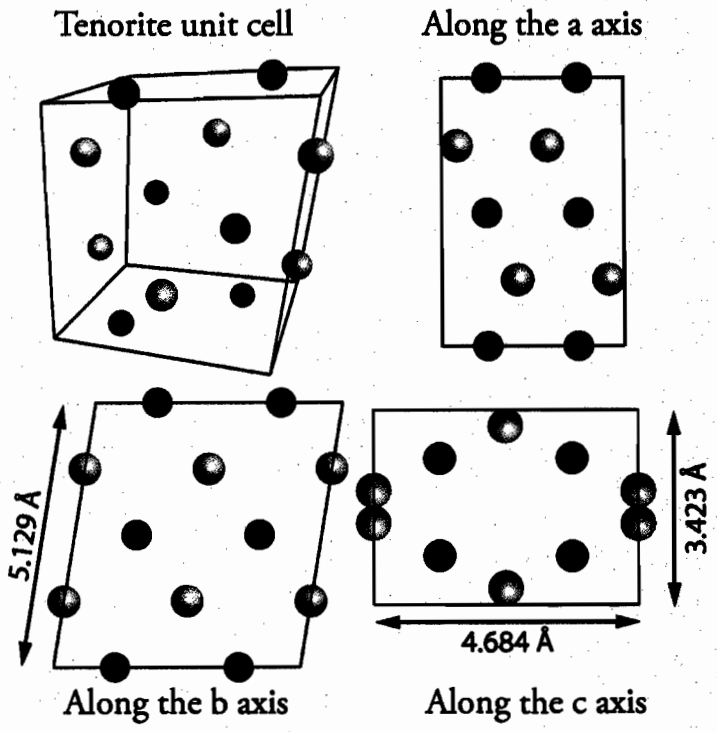

Figure 5.2: *A 3D image of the unit cell of tenorite (CuO) is given in the upper left corner. Views along each of the crystal axes, together with the lattice parameters, are also displayed. The copper has a valence state of 2+ in this structure. Oxygen is represented by the larger lighter colored spheres and copper by the smaller darker colored spheres.*

the copper atoms are on the vertices of a tetrahedron around each oxygen atom. A schematic representation of the unit cell is shown in figure 5.1 on the facing page.

When Cu_2O is oxidized further copper becomes Cu^{2+} and the final composition is CuO, which is also known as tenorite and has space group $C2/c$. CuO has a monoclinic unit cell and each atom has four nearest neighbors of the other kind: the oxygen atoms are in the center of a distorted copper tetrahedron and the copper atoms are in the center of oxygen rectangles.[3] The unit cell of CuO is depicted in figure 5.2.

Between Cu_2O and CuO there is another phase that can form, namely Cu_4O_3 or paramelaconite. In this metastable phase the copper ions have a mixed valence: some are 1+ and some are 2+. Datta and Jeffrey[4], O'Keeffe and Bovin,[5] and Morgan *et al.*[6] have determined that the unit cell has tetragonal symmetry, space group $I4_1/amd$, with $a = 5.818$ and $c = 9.894$ Å and unit cell contents $Cu_2^{2+}Cu_2^{1+}O_3$.

We will not consider further oxidation of the Cu to 3+, because of the following arguments, which were proposed by Geballe and Koster.[7] Those authors compare Cu in a crystal lattice to Cu in a aqueous solution, a comparison that is allowed because in both the crystal lattice and the aqueous solution the cations are coordinated by

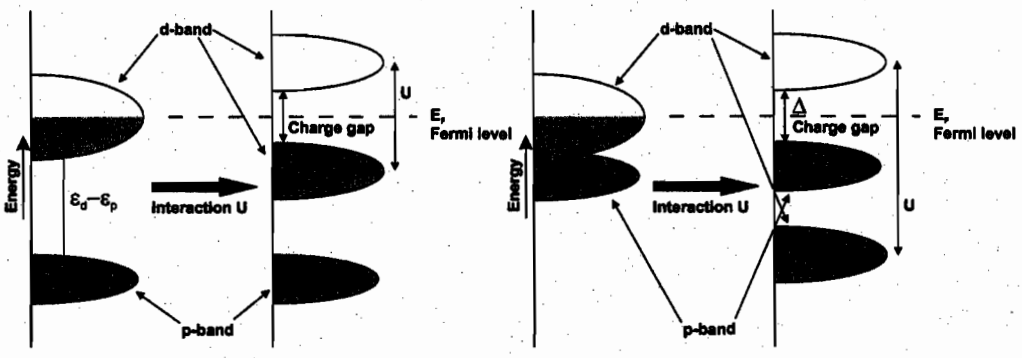

Figure 5.3: *Schematic illustration of the energy levels for a Mott-Hubbard insulator (left) and a charge-transfer insulator (right). The interaction on the d-site results in a splitting of the d-band and a charge gap formed by the upper and lower Hubbard band in the Mott-Hubbard insulator case or the upper Hubbard band and the p-band in the charge-transfer case. After Imada, Fujimori, and Tokura.*[20]

charges in these materials cannot flow freely when a *dc* electric field is applied, but instead undergo polarization. Conventional electronic structure techniques do not yield the right answer in all cases as they do not take strong electron correlation effects into account. In classical physics the difference in behavior when cooling down was explained by looking at the state of the electronic charges: they are either *bound* or *free*, corresponding to the Lorentz model for insulators and Drude model for metals respectively. When quantum physics is considered the distinction between the two states is no longer so obvious. The most used model to calculate electronic properties is the electronic band model: the band structure and the position of the Fermi level determine the behavior of the material.[17] In many materials, such as ionic insulators, simple metals, and some semiconductors, the band structure model and the related Fermi liquid description provide a good explanation of their physical properties. Insulators have only filled and empty bands in the band model, whereas metals have one or more partially filled bands. The assumption made in the band model is that electron interaction is limited to weak interactions. When Coulomb interactions become dominant in a system, immobilization of the electrons can occur for certain band fillings: these are commensurate fillings, for example $\frac{1}{2}$ filling. The insulators for which this is the case are called Mott insulators (after N.F. Mott who first described these materials in 1949).[18] Examples of Mott insulators are GaAs quantum wires, organic Bechgaard salts, undoped high-temperature superconductors,[19] and transition metal compounds including CuO. The interactions between the electrons can lead to novel phases which are strongly influenced by the carrier concentration as varied by doping away from half filling; an overview is provided by Imada, Fujimori, and Tokura.[20]

In a band insulator the conductivity is blocked by the Pauli exclusion principle: the electrons cannot move because the bands are fully filled (two electrons per unit cell). In a Mott insulator charge conduction is blocked by Coulomb repulsion. Every site contains a single electron, so when a second electron tries to hop to another site it

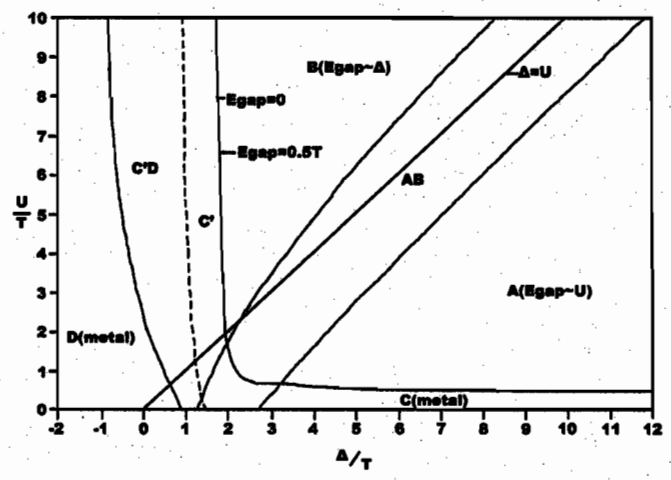

Figure 5.4: *The phase diagram by Zaanen, Sawatsky and Allen[22] classifies the various regions as a function of U and Δ. The various regions are: (A) The Mott-Hubbard insulators, where the energy gap (U) is formed by the d-band. Holes and electrons have a d character and are both heavy; (B) Charge-transfer insulators, where the energy gap (Δ) is formed by the p-band and the upper Hubbard band and is proportional to the electronegativity of the anion. Holes are light (p-band) and electrons are heavy (d-band); (AB) The intermediate region between the previous two, where holes are of intermediate mass and electrons are heavy; (C) d-band metals, where electrons and holes are both heavy; (D) p-type metals, which have holes in the anion valence band (light holes); (C'D) Intermediate region between the previous two regions.*

encounters the electron that was already there. This results in electron-electron repulsion, and when this repulsion is strong enough (roughly when the Coulomb interaction is larger than the bandwidth) all charges are fixed in the material, resulting in an insulator.

A good way to describe materials in which correlation dominates the transport properties is the Mott-Hubbard model. The Mott-Hubbard model proposes that charge fluctuations (with energy U) of the type $d_i^n d_j^n \leftrightarrow d_i^{n-1} d_j^{n+1}$ (where i and j label transition-metal sites) form the band gap; for CuO this would be $d_i^9 d_j^9 \leftrightarrow d_i^8 d_j^{10}$. This is correct for the light transition metal compounds, such as those of Ti and V. For the Co, Ni and Cu compounds however the gap does not seem to be a d–d gap, but is directly related to the electronegativity of the anion and is therefore of a charge transfer type.[21] This type of charge fluctuation does not involve U, but the charge transfer $d_i^n \leftrightarrow d_i^{n+1}\underline{L}$ (for CuO: $d_i^9 \leftrightarrow d_i^{10}\underline{L}$ with energy Δ), where $\underline{L}$ denotes a hole in the anion (oxygen in CuO) valence band. A schematic illustration of the energy levels for Mott-Hubbard and charge transfer insulators is given in figure 5.3 on the previous page. In going from lighter to heavier transition-metal elements, the d level is lowered and therefore Δ is decreased, whereas U is increased because the spatial extend of the d orbital shrinks with the atomic number. This results in compounds containing a light transition-metal to become Mott-Hubbard insulators, whereas compounds containing a heavy transition

metal become charge-transfer type insulators. The electronegativity of the anion only influences Δ, higher electronegativity means Δ is decreased. Zaanen, Sawatzky and Allen[22] constructed a phase diagram that orders $3d$ transition-metal compounds with respect to the energies U and Δ. This phase diagram is given in figure 5.4 on the facing page. Whether doped carriers in a filling controlled system have oxygen p-band character or transition-metal d-band character is an important question in considering the transport properties of transition metal oxides. Doped holes have a d-band character in Mott-Hubbard insulators and a p-band character in charge-transfer insulators. Doped electrons have a d-band character in both cases, because the conduction band has a d character in both cases.

Ghijsen *et al.*[23] show that tenorite is a charge transfer gap insulator. NiO has a rocksalt structure and is also a charge transfer gap insulator, it can therefore be expected that CuO in a rock salt structure will be a charge transfer gap insulator as well. A summary of the electronic parameters of the oxides can be found in table 5.2.

Photoemission spectra

A direct way to measure the band structure is by performing PES. This section will describe the core level photoemission spectra of Cu, Cu_2O and CuO. It will focus on the $2p$ doublet of Cu, since it carries most information about the oxidation state of copper and on every sample made as part of this work these peaks have been measured. Examples of these spectra are given in figure 5.5 on the following page. For Cu and Cu_2O only two peaks appear: the $2p_{\frac{3}{2}}$ and the $2p_{\frac{1}{2}}$, which can be linked to $2p^5 3d^{10}$ final state. For CuO two extra satellite peaks appear, which are characteristic of the formation of a $2p^5 3d^9$ final state. Such satellite structures are also visible in the spectra of the copper dihalides[32] and nickel metal.[33] The ground state of copper is a $3d^9$ state and the main peaks related to the $3d^{10}$ state are not expected to have any intensity. Due to the hybridization of the bands the oxygen can donate an electron to the copper to create a lower energy state, which is denoted by an $\underline{L}$ indicating a hole on the ligand. The main peaks are therefore denoted as $2p^5 3d^{10}\underline{L}$ final states. The main peak is also a lot broader for CuO than it is for Cu or Cu_2O, which has been explained by Van

	Cu	Cu_2O	CuO
Resistivity at 300 K ($\mu\Omega$ cm)	1.7	6.2×10^8	10^9
Bandgap (eV)	n/a	2.1	1.4
Cu $2p$ binding energy (eV)	932.4 ± 0.1	932.3 ± 0.2	933.5 ± 0.3
O $1s$ binding energy (eV)	n/a	530.3 ± 0.3	529.5 ± 0.2

Table 5.2: *Summary of the electronic properties of Cu, Cu_2O, and CuO in numbers: the resistivity at room temperature, the bandgap, and the positions of important core level XPS lines. For CuO there are additional parameters related to the strong electron correlation:*[23,24] *the copper–oxygen charge-transfer energy $\Delta = 1$ eV, the d–d Coulomb interaction $U = 7$ eV, and the ligand–d hybridization $T = 2.4$ eV. For the XPS lines an average of the values found in literature is given and the standard deviation.*[23,25,26,27,28,29,30,31]

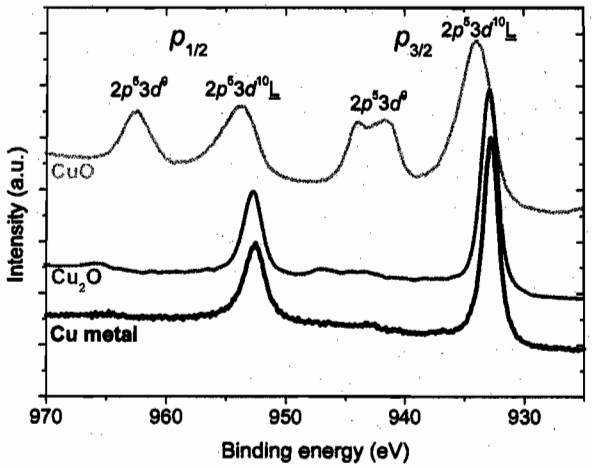

Figure 5.5: *Photoemission spectra of Cu, Cu_2O, and CuO (tenorite). For both Cu as well as Cu_2O only 2 peaks are visible, which are related to the $2p^5_{3/2}3d^{10}$ and the $2p^5_{1/2}3d^{10}$ final states, which have almost the same binding energy in both materials. The CuO spectrum is more complex and has 4 peaks due to the possibility of oxygen donating an electron to the copper 3d band. The final states for the CuO peaks are labeled in the figure. The largest peak is called the main peak and the smaller peak related to the ground state is called the satellite peak in the text. The peaks of the CuO are shifted to higher binding energy by more than 1 eV. They are also much broader than the peaks of the other two materials due to delocalized screening and multiplet splitting, which is explained in the text.*

Veenendaal and Sawatsky.[34,35] By performing calculations they show that there is a competition between screening electrons coming from local ligand atoms and electrons coming from ligand atoms of neighboring Cu metal ions to screen the charge on the Cu. This causes an extra contribution to the main peak, which shows up as a shoulder at higher binding energy in the case of CuO. The multiplet splitting in the $2p^53d^9$ satellite peak is more subtle and is the subject of many papers.[36,37]

5.1.3 Magnetic properties

The electrons in a Mott insulator cannot move, but their spins can still fluctuate. The spins usually arrange themselves in an antiparallel fashion, due to virtual charge fluctuations,[38] which leads to long-range antiferromagnetic ordering. The temperature at which this ordering takes place is the Néel Temperature (T_N).

The Néel temperatures for transition metal monoxide compounds with a rock salt structure are graphically represented in figure 5.6 on the next page. The y-axis is scaled logarithmically and the Néel temperature increases exponentially with the transition element number. The Néel temperature for CuO does not follow this trend, but remember, CuO has a monoclinic structure. If CuO could be forced into a rock salt structure its Néel temperature would be slightly higher than 800 K based on a linear extrapolation. A recent theoretical exploration of the Néel temperature in these

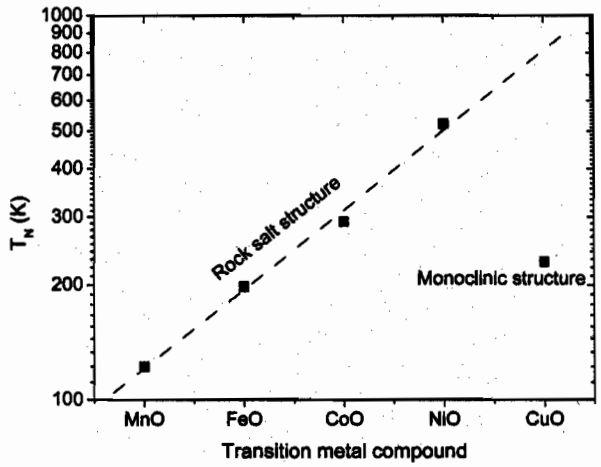

Figure 5.6: *An overview of the Néel temperatures for transition metal monoxides with a rock salt structure. T_N increases exponentially with each element up to NiO as indicated by the dashed line, which is a fit of the first four points. The T_N of the monoclinic CuO structure does not follow this trend, but is much lower. When a rocksalt structure of CuO is formed T_N might follow the trend and linear extrapolation predicts a T_N slightly higher than 800 K.*

materials was performed by Harrison.[39]

The Néel temperature in these materials in thin films is also a function of thickness, which has been observed both experimentally[40,41] as well as theoretically.[42] For NiO the Néel temperature is reduced from 520 K for bulk material to 470, 430, and 295 K for 20, 10 and 5 monolayer films respectively, as measured by x-ray absorption spectroscopy.[40] This thickness effect is due to uncompensated moments at the surface causing disorder and can be modeled as a finite-size effect.[43] The reduction of the Néel temperature with thickness is quite substantial in transition metal monoxides compared to other compounds.[44] A reason for this strong dependence in NiO may be found in the crystal structure. In a rocksalt structure the nearest-neighbor (100) layers are not or hardly coupled via the superexchange interaction because of the 90° Ni-O-Ni bonds, while the next-nearest-neighbor layers are only coupled by one 180° superexchange path. Due to this weak coupling the bulk Néel temperature will only be reached for fairly thick layers of NiO. A similar dependence is to be expected for CuO when it is stabilized in a rock salt structure.

Measuring the Néel temperature or the magnetic properties of an antiferromagnetic thin film in general is not easy due to the antiparallel arrangement of the spins which means the long range magnetic signal averages to zero. The usual way of determining the Néel temperature for bulk samples is to measure heat capacity, a method which is not suitable for very thin films. A good example of heat capacity measurements on doped CuO is the work by Saito *et al.*[45] Another bulk technique is the use of neutrons to determine spin alignment and has to be performed at specialized facilities. However, more material than is present in our thin films is needed to gather reliable

data. Bulk data of this type is available on a lot of transition metal compounds, for example the work by Roth on the transition metal monoxides.[46] In somewhat thicker films measuring the dc-susceptibility is a good option. After the transition to the antiferromagnetic state the susceptibility will drop sharply, which can be seen in CoO/SiO2 multilayers by Ambrose and Chien.[43] For thinner films there are some synchrotron related techniques. The first one is x-ray absorption spectroscopy (XAS). Alders *et al.*[40] calculate that the Ni L_2-XAS in NiO is dependent on the presence exchange interaction. This way those authors measure the Néel temperature in NiO films as thin as 5 ML. The second synchrotron technique is x-ray magnetic linear dichroism spectroscopy (XMLD). Here linearly polarized x-rays are used to probe the expectation value of the square of the magnetic moment, $< M^2 >$, because linearly polarized photons have only axiality. Because linearly polarized light is used, in contrast to circularly polarized light, any uniaxial magnetic system can be measured, which includes antiferromagnets. In the right setup this technique measures only the top 2 nm of a film, making this a very suitable technique for very thin films. The merits of this technique were demonstrated by Stöhr and coworkers on a film of NiO.[47] The last technique we will discuss here is measuring the transition temperature by using the exchange bias effect. The exchange bias effect, which was discovered in 1956,[48] exists at the interface between a ferromagnet and an antiferromagnet. It will be discussed in more detail in the following paragraphs, since we will come back to it later in the chapter.

Ferromagnets have a large exchange parameter, but a relatively small anisotropy, which makes the ferromagnetic ordering stable at high temperatures, but the orientation may not be stable. Most ferromagnets have two equally favored magnetic directions which are collinear and lie along the so-called easy axis. Antiferromagnets on the other hand have a very large anisotropy and therefore have very stable orientations.

When an interface is formed between a ferromagnet and an antiferromagnet the exchange coupling can result in the existence of ferromagnetic behavior with stable order and high anisotropy.[49] This phenomena is called the exchange bias effect and influences the shape and position of the magnetic hysteresis loop. When a ferromagnet is grown on top of an antiferromagnet the exchange coupling between the two systems only leads to an increased coercivity of the ferromagnet. This is usually attributed to the increased coercivity of *interfacial spins* which need to be dragged around by the external field. However, the ferromagnetic hysteresis loop is still symmetric, indicating two equivalent easy directions.

When cooled down in a magnetic field on the other hand the hysteresis loop is no longer centered around zero magnetic field. These shifts are most easily observed when perfect interfaces are formed and the Néel temperature of the antiferromagnet is lower than the Curie temperature of the ferromagnet. In that case a magnetic field is applied to the heterostructure above the Néel temperature and the sample is then cooled down to below the Néel temperature in a magnetic field. In this case the layers of the ferromagnet closest to the interface will be pinned in a uniform direction and a shift in the hysteresis loop results.

The condition of $T_N < T_C$ may not be satisfied in our materials system, because we do not know the Néel temperature of the new phase, and a more disordered system

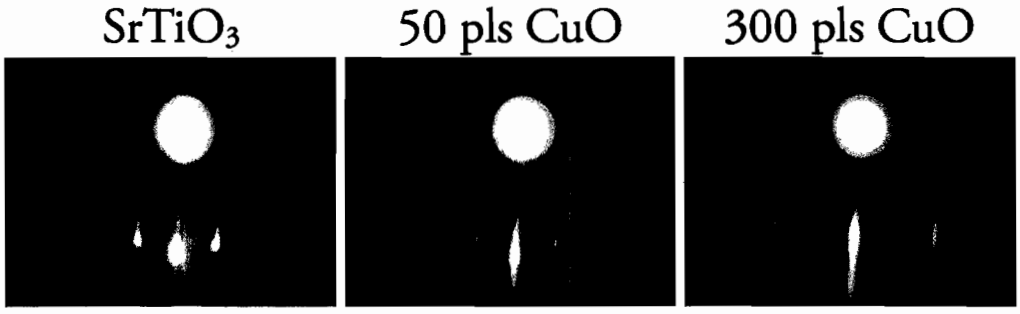

Figure 5.7: *The evolution of the RHEED spectrum during the growth of CuO on $SrTiO_3$ taken along the (01) direction of $SrTiO_3$ shows a transition from a clear 2D pattern for bare $SrTiO_3$ on the left to the streaky pattern of CuO on the right. 300 pulses of CuO corresponds to a 15 – 20 Å thick film.*

might result. This disorder can come from structural defects, but also from the formation of domains in the ferromagnet and the antiferromagnet.[50] The measurement can, therefore, be an average over many such domains and may not show a shift in the hysteresis loop. The magnitudes of the coercive and exchange bias fields are a function of the thickness of the antiferromagnetic layer, which is most likely due to a change in its domain structure.[51,52] Much work has been done recently on describing exchange bias effects at interfaces[53] and so far the Mauri-Siegmann model[54] seems to offer the best fit with observations. If a rock salt structure of CuO can be formed it might behave a lot like NiO, which is the transition metal compound closest to it. NiO is known to exhibit weak bias fields, probably due to the relatively small magnetocrystalline anisotropy (i.e., NiO is not a very hard antiferromagnet).

Measuring the Néel temperature by the exchange bias effect is further complicated by the so-called blocking temperature, T_b. At T_b the exchange bias field, i.e. the shift in the hysteresis loop, approaches zero and T_b is a measure for the thermal stability of the exchange bias. The blocking temperature is always lower than the Néel temperature and has been shown to be a function of the thickness of the antiferromagnetic layer.[55]

5.2 Epitaxially strained growth on $SrTiO_3$ and characterization

It is possible to grow CuO with a higher degree of symmetry (tetragonal) by depositing on $SrTiO_3$ and thereby making use of epitaxial strain. The next few sections offer an overview of the findings on this new tetragonal phase of CuO. The results on growth, structure, electronic properties, and magnetic properties are presented.

5.2.1 Growth

Samples were either grown on $SrTiO_3$ or on doped, conducting $SrTiO_3$, where the doping was 0.5% Nb. The latter offers the advantage of reduced charging when performing

PES on the insulating CuO samples. Both kinds of substrates were TiO_2 terminated, as described in section 2.3.1 on page 13.

In order to stabilize the new phase it is of utmost importance to oxidize Cu to a 2+ state. This is accomplished by using a target of CuO and providing atomic oxygen with the source operating at 600 W with a flow of 2.5 sccm oxygen resulting in a background pressure in the system of 1.5×10^{-5} Torr. The temperature of the substrate was kept constant at 600 °C and the growth was monitored by RHEED. The RHEED patterns in figure 5.7 on the previous page show a sequence of events in the case of perfect growth. A streaky pattern emerges from the CuO, without any 3D spots between the streaks. Figure 5.8 contains a pattern that shows what happens when the film relaxes to tenorite, which is clearly different from the new CuO phase.

When grown on dual terminated substrates the growth was found to be more 3D and the films relaxed to the tenorite phase at an earlier stage. Similar effects were observed on other substrate materials, such as $DyScO_3$ and $LaAlO_3$, where 3D growth patterns dominated. Those substrates are double terminated by nature and no known reliable methods exist to make them single terminated, an effort further complicated by the polar nature of these materials (for more information on polar materials see chapter 3 on page 27). These other substrates have different lattice parameters as well, which influence the stress put on the material.

The films were not always stable in atomic oxygen below 300 °C, when cooled after deposition. The films, it was found, would relax to tenorite when cooled to room temperature under deposition conditions. For this reason the atomic oxygen was switched off at 300 °C and the sample was cooled to room temperature in molecular oxygen ($\sim 10^{-5}$ Torr). This implies that the stability line for the tetragonal CuO when exposed to atomic oxygen lies at 300 °C.

The thickness of the tetragonal CuO samples is limited by a relaxation to the tenorite phase when growing beyond a certain thickness. For most samples 300 laser pulses were used in the PLD process to guarantee a streaky RHEED pattern with no 3D spots. This corresponds to a layer thickness between 15 and 20 Å. AFM imaging

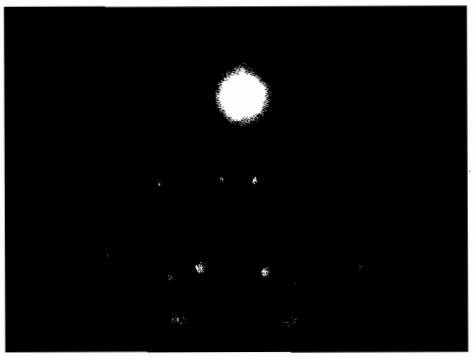

Figure 5.8: *The RHEED spectrum during the growth of tenorite CuO on $SrTiO_3$ taken along the (01) direction of $SrTiO_3$ showing clear 3D spots.*

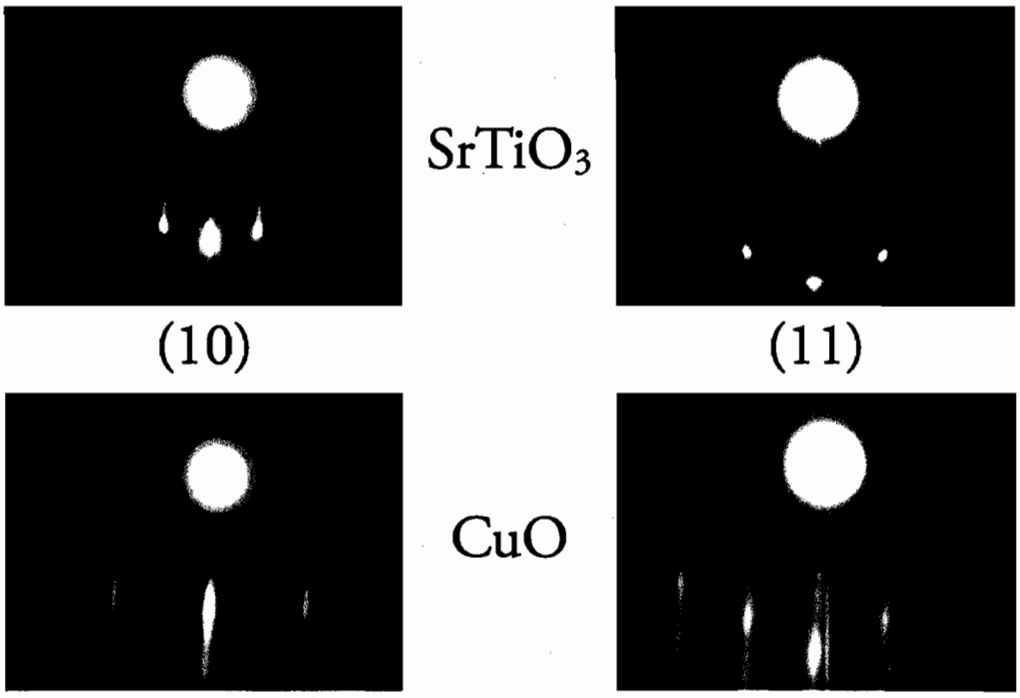

Figure 5.9: *The electron diffraction patterns of $SrTiO_3$ and CuO taken along their (10) and (11) directions. Even though the (10) reflection of CuO is not allowed as explained in the text, very faint lines at its position are usually visible. The patterns shown here are both fourfold symmetric when the sample is rotated around its azimuthal axis.*

confirms that thin samples are flat with the $SrTiO_3$ step structure still visible, whereas the samples that are thicker have "particles" on top, associated with the film growth process, that would cause a 3D pattern to appear.

5.2.2 Structural properties

To confirm the growth of a new phase the first thing to determine is its structure. The in-plane lattice parameters could be deduced from the RHEED spectra, which were taken during growth. The out-of-plane lattice parameter is more difficult to measure due to the limited amount of material with which to work. Through the application and simulation of XPD spectra we have been able to construct the unit cell of the new phase. First the in-plane and subsequently the out-of-plane parameters are discussed.

In-plane lattice parameters

To determine in-plane lattice parameters of the new phase RHEED spectra were used. Spectra taken along the $SrTiO_3$ (10) and (11) are shown in figure 5.9, and since the lattice parameters of the $SrTiO_3$ are well known (3.905 Å cubic), those of the CuO can

be calculated by comparing to $SrTiO_3$. When this data is taken at face value and this method is used on the spectra that are displayed, one calculates a distance of 1.92 Å along the $SrTiO_3$ (10) direction and 2.72 Å along the (11) direction. This suggests that the unit cell of the new CuO phase is 45 degrees rotated with respect to the $SrTiO_3$ if we assume a rock salt structure, i.e. the (11) direction of CuO is parallel to the (01) direction of $SrTiO_3$. The result would be a unit cell with as many atoms as the tenorite unit cell, but with only a quarter of the volume, and the Cu–O bond length would be 1.36 Å, a seemingly unphysical value. However, for a rock salt structure, in 3D as well as 2D, not all the diffraction peaks are allowed, as can be seen from the following calculations.

In a face centered crystal lattice every atom with coordinates (x, y) has one identical atom with coordinates $(x + \frac{1}{2}, y + \frac{1}{2})$. For every unit cell with n atoms there are $n/2$ groups of two atoms. The structure factor can be written as a summation of such groups of two:

$$F_{hk} = \sum_{n/2} \{ f_n e^{2\pi i(hx_n + ky_n)} + e^{2\pi i(h(x_n + \frac{1}{2}) + k(y_n + \frac{1}{2}))} \}$$

And can also be written as:

$$F_{hk} = [1 + e^{\pi i(h+k)}] \sum_{n/2} f_n e^{2\pi i(hx_n + ky_n)}$$

The part of the equation before the summation takes the value 2 if h and k are unmixed, both odd or both even, and 0 when they are mixed:

$$\text{h,k unmixed: } F_{hk} = 2 \sum_{n/2} f_n e^{2\pi i(hx_n + ky_n)}$$

$$\text{h,k mixed: } F_{hk} = 0$$

In 3D the result is similar, but then for three dimensions: h, k, and l. The absence of l does make a difference though; the (330) reflection, for instance, would not be allowed in three dimensions, but in two dimensions it becomes (33) and is allowed. For the analysis of the RHEED patterns this results in the (01) reflection not being allowed, but the (11) is allowed and therefore the shortest spacing between the diffraction peaks now corresponds to the (11) direction.

Applying these insights allows us to calculate the correct in-plane lattice parameters. In the (11) direction of the $SrTiO_3$ substrate the (11) and (22) reflections of CuO are allowed, and along the (01) direction of the $SrTiO_3$ the (02) and (04) reflections of CuO are allowed. The CuO in-plane lattice parameters are exactly the same size as the $SrTiO_3$ underneath. This corresponds to a Cu–O bond length of 1.95 Å in-plane, a number which corresponds well with values found in high T_c materials or in monoclinic CuO. If the unit cell were cubic this would result in a unit cell volume of 59.5 Å, still shy of the 81.1 $Å^3$ of tenorite. To solve this discrepancy the unit cell could be elongated along the out-of-plane direction, but based on the RHEED spectra alone we cannot

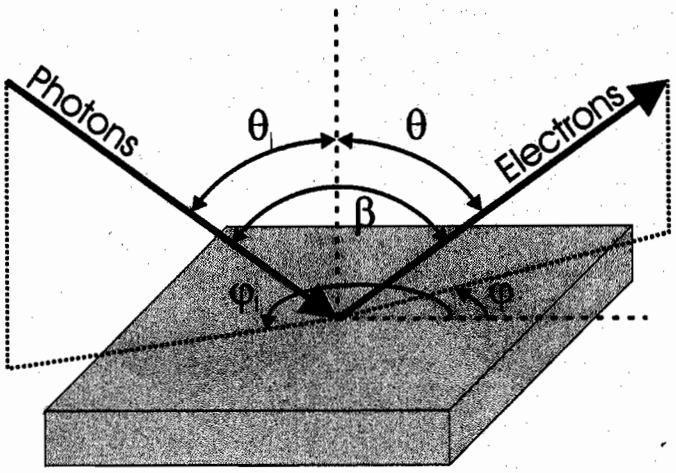

Figure 5.10: *A schematic layout of the XPD setup and the important angles, which are mentioned in the text. The angles the incident beam makes with respect to the sample have a subscript i. θ is the angle between the detector and the surface normal and φ is the angle between the detector and one of the in-plane crystal axes of $SrTiO_3$. In our setup only the sample moves and therefore $\theta + \theta_i = \beta = 45°$.*

draw any conclusions about the out-of-plane lattice constant, which is the subject of the next section.

Out-of-plane lattice parameters

To measure the out-of-plane lattice parameter we employed XPD (see section 2.4.1 on page 18). To verify that the technique would produce reliable results it was first applied to a conducting 0.5% Nb-doped $SrTiO_3$ substrate. For this measurement the energies were fixed on the Ti $2p$, Sr $3d$, and the O $1s$ peaks and a pass energy of 100 e V was set. The acceptance angle for electrons was 5 degrees and the peak heights were measured every 2° for θ and every 3° for ϕ resulting in a matrix of 3600 points. The results are displayed in figure 5.11 on the following page, and for each of the elements a clear modulation of intensity, as a function of angle, is visible. The simulations were performed with software by Abajo *et al.*[56] with the following key parameters:

- a cluster of 1247 atoms;
- incoming linear polarized light parallel to the surface;
- a surface potential of 10.5 eV;
- an electron inelastic mean free path of 23 Å for O and Ti, and 29 Å for Sr;
- 20 orders recursive iteration;
- a maximum orbital quantum number of 20;
- a sample temperature of 350 K;

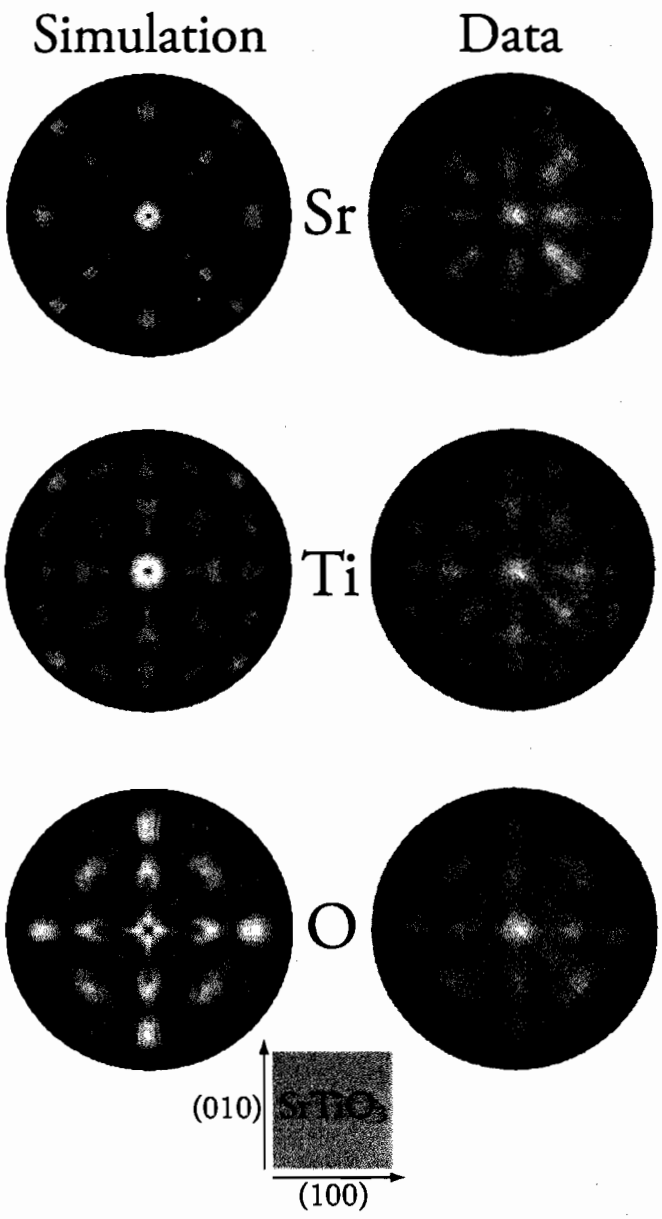

Figure 5.11: *Simulated and measured XPD patterns for each of the elements in $SrTiO_3$: Sr 3d, Ti 2p, and O 1s. The simulations were generated using the parameters mentioned in the text. The measurements were performed with the pass energy set at 100 eV, an acceptance angle of 5 degrees in steps of 2° for θ and 3° for ϕ. The correspondence between the simulation and the measurement is good for low angles of θ, whereas some detail is lost in the measurements at high angles due to less than optimal alignment of the sample at high angles.*

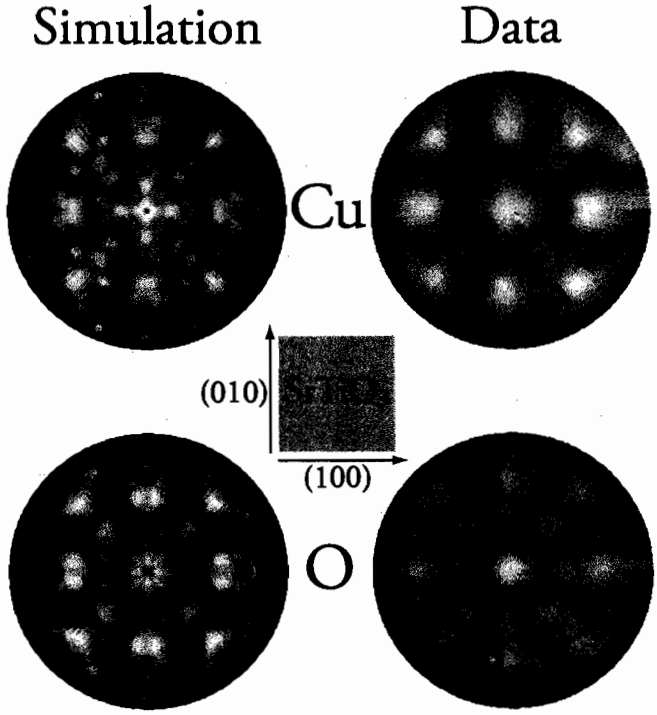

Figure 5.12: *XPD patterns for CuO measured (on the right) at two binding energies: the O 1s and the Cu $2p_{\frac{3}{2}}$ main line. The measurements were performed with the pass energy set at 100 eV, an acceptance angle of 5 degrees in steps of 2° for θ and 3° for ϕ. Simulations of the CuO in tetragonal form are shown on the left, as calculated with the parameters mentioned in the text. The Cu signal comes solely from the film, whereas the O signal has a significant contribution from the substrate. The Cu pattern shows clear four-fold symmetry, which is not what would be expected from a single domain tenorite film.*

- a Debye temperature of 400 K;
- an emission angle window of 5 degrees.

The values for the electron inelastic mean free path were determined with the aid of the NIST IMFP database.[57] The similarity between the simulations and the measured data is clearly visible, which validates the use of this technique.

The technique was then applied to CuO and two energies were measured: the O 1*s* and the Cu 2*p*. For the O signal a mixture of the substrate and the film is to be expected since the escape depth of the electrons is higher than the thickness of the CuO layer. The copper signal comes solely from the film because the substrate contains no copper. The copper pattern shows a fourfold symmetry as shown on the right in figure 5.12, which is indicative of a fourfold symmetric unit cell, such as a rock salt structure. The simulation shown on the left of the figure looks strikingly similar to the

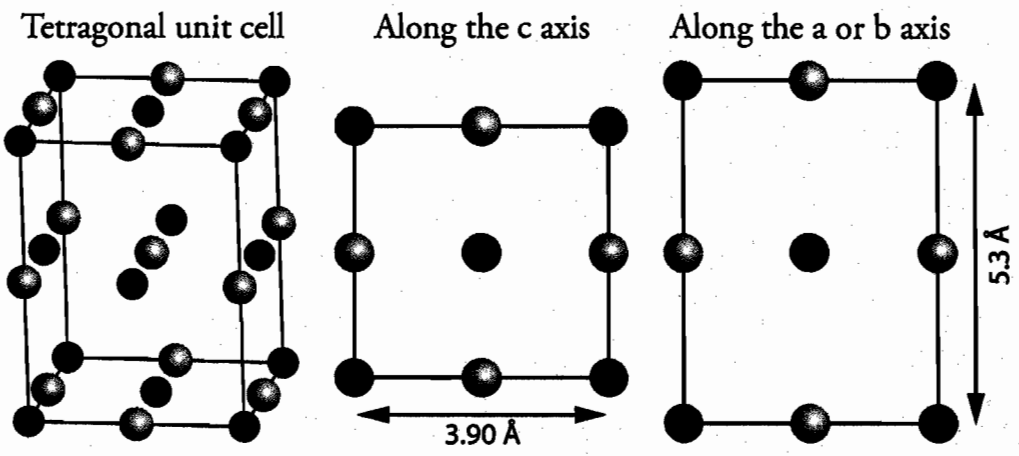

Figure 5.13: *The unit cell of the tetragonal phase of CuO as it is stabilized on $SrTiO_3$. An orthographic representation of the unit cell on the left and views along the c and a or b axes to the right of that. The lattice parameters are given along the respective directions. The Cu atoms are represented by the smaller darker colored spheres and the O atoms by the larger lighter colored ones.*

measurement, which has been accomplished by using the following parameters:

- a unit cell with $a = b = 3.905$ and $c = 5.320$ Å;
- a rock salt structure with 8 atoms per unit cell;
- a cluster of 1505 atoms;
- incoming linear polarized light parallel to the surface;
- a surface potential of 10.5 eV;
- an electron inelastic mean free path of 10.5 Å for Cu, and 21 Å for O;
- 20 orders recursive iteration;
- a maximum orbital quantum number of 20;
- a sample temperature of 350 K;
- a Debye temperature of 400 K;
- an emission angle window of 5 degrees.

The unit cell dimensions mentioned above results in a unit cell volume of 81.1 $Å^3$ which is the same as for tenorite. Using the XPD data, the out-of-plane lattice parameter cannot be determined more accurately than this. The shortest Cu–O bond length in this structure is 1.95 Å, which corresponds to the value found in tenorite. The shortest Cu–Cu and O–O bond lengths are 2.76 Å, a value that is in between the values found for the two in tenorite. A schematic drawing of the unit cell is given in figure 5.13 together with the lattice parameters.

5.2.3 Electronic properties

When the structure of CuO is changed from monoclinic to tetragonal we expect a change in the electronic structure of the material. This should influence the core electrons of copper and therefore the shape of the Cu $2p$ lines in XPS. The XPS spectra of the Cu $2p$ lines for both the tenorite as well as the tetragonal structure are presented in figure 5.14 on the next page. For tenorite we find 933.5 eV for the binding energy of the Cu $2p_{\frac{3}{2}}$ and 529.4 eV for the O $1s$, which corresponds well to values found in literature (see table 5.2 on page 83); the energies do not appear to change significantly in spectra of the tetragonal phase. Compared to the tenorite spectrum, the tetragonal CuO spectrum has a larger shoulder on the main peak at higher binding energy, a narrower satellite peak, and the spectral weight of the first satellite peak has shifted to lower binding energy. More precisely, when going from the monoclinic to the tetragonal phase the fwhm of the main peak increases from 3.6 to 4.1 eV, whereas the fwhm of the satellite peak decreases from 4.5 to 4.2 eV.

After exposure to air the top layer of the CuO was found to degrade to tenorite. This has been examined by using angle dependent XPS. In figure 5.15 on the next page, the spectra taken at 90 and 30 degrees (the angle between the detector and the sample surface) are plotted. At 90 degrees more electrons from greater depth reach the detector and the spectrum of the tetragonal phase is clearly visible. At 30 degrees the electrons come more from the top surface layer and a tenorite spectrum is measured. The top layer is therefore mostly tenorite, whereas the layer closest to the interface with $SrTiO_3$ is mostly tetragonal. When the sample is kept under vacuum after growth, the CuO is slowly reduced over a period of days. After four days the intensity of the satellite peaks are reduced to about half their size after deposition.

Now we turn to the valence bands of the tetragonal CuO. The valence bands were measured with He I radiation; the results are presented in figure 5.16 on page 97. The spectrum is very similar to that obtained on tenorite by other groups.[23,58,59,24,60] For example, there are no states at the Fermi level, which is as expected for an insulator. There are some notable differences though. The peak at low binding energy (~1.9 eV), which is caused by both oxygen and copper,[61] is not as strong in our spectrum as it is in spectra of tenorite. The largest peak, caused mainly by copper, clearly consists of two separate peaks in our spectrum, which has not been observed before for tenorite. Calculations on the tenorite band structure show a splitting of this peak though[23,61] and in some measurements a clear shoulder is visible.[58] The peaks at 5.8 and 7.0 eV are both oxygen peaks and are also predicted by calculations.[61] The double peak feature at higher energy (10-13 eV), which also exists for tenorite, is a copper feature only predicted by the most advanced calculations.[59,62,61] All calculations predict the peaks to be at lower binding energies than measured here. Compared to most calculations on tenorite the spectrum presented here is shifted up by as much as 2 eV. Compared to experiments performed on tenorite, the spectrum for the tetragonal phase is shifted to higher binding energies by about 0.5 eV. For a film of this thickness a contribution of the substrate to the spectrum is expected and some states present at the Fermi level seem to confirm this. $SrTiO_3$ has two large peaks at higher energies (4.4 and 6.6 e V), but no clear correlation between these peaks and the measured spectrum has been

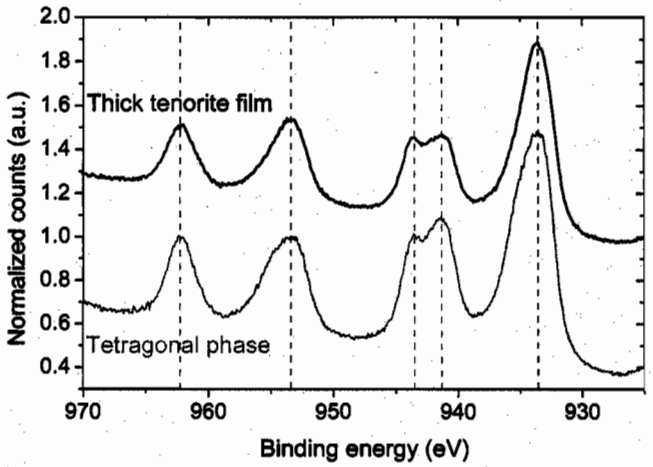

Figure 5.14: *The Cu 2p core level XPS spectrum of the tetragonal CuO looks significantly different from the tenorite spectrum. The most striking differences are the broadening of the main peak, the narrowing of the satellite peak, and the redistribution of weight in the satellite peak. The spectra have been normalized on the $2p_{\frac{1}{2}}$ peak and the tenorite spectrum has been given an offset for clarity.*

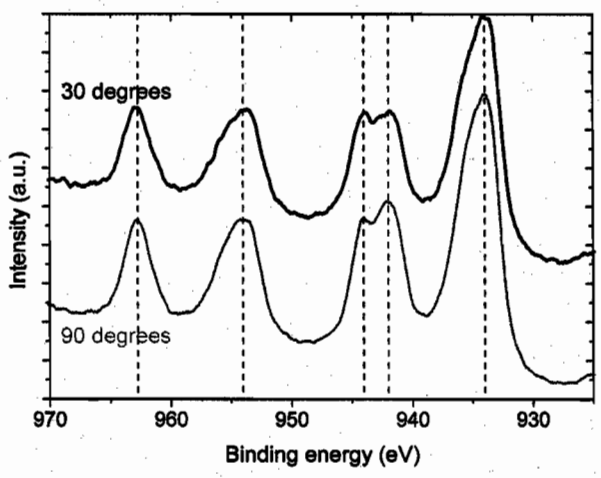

Figure 5.15: *Two Cu 2p core level XPS spectra taken on the same sample at two different angles with respect to the analyzer after exposure to air. At 90 degrees the sample normal faces directly towards the electron analyzer, whereas at 30 degrees there is a 60 degree angle between the surface normal and the electron analyzer. The spectrum taken at 30 degrees looks more like the tenorite spectrum from figure 5.14, although the width of the peaks is still different from those of tenorite. The two spectra are normalized to the intensity of the main peak and the spectrum taken at 30 degrees has been given an offset for clarity.*

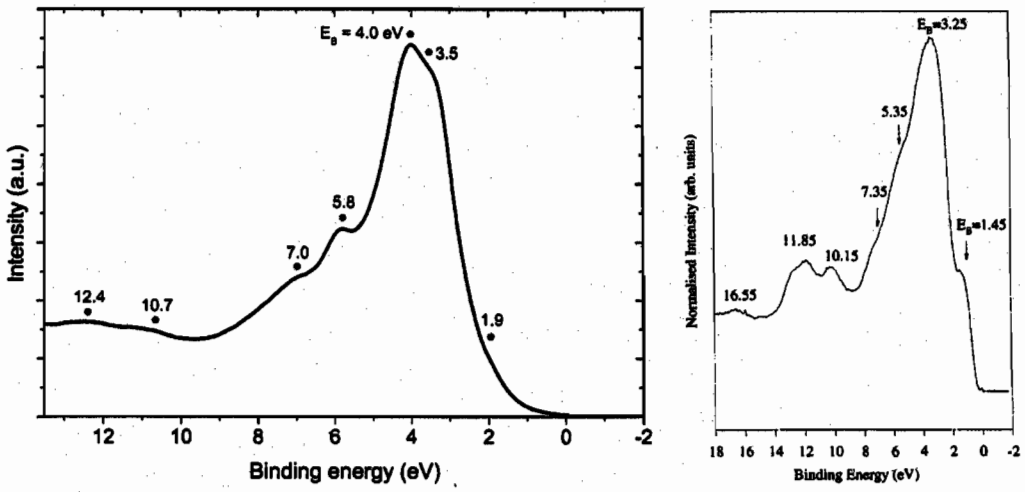

Figure 5.16: *The tetragonal CuO valence band spectrum, on the left, measured with HeI radiation. The Nb doped $SrTiO_3$ substrate contributes to the spectrum for such thin films, but its contribution is expected to be very small. On the right is a typical tenorite spectrum taken at 70 eV radiation and the peak positions, by Warren et al.*[60]

found.

5.2.4 Magnetic properties of tetragonal CuO

In order to determine the magnetic properties of the CuO films the exchange bias effect of CuO films grown on thin $SrRuO_3$ on $SrTiO_3$ was measured. $SrRuO_3$ was chosen because of its close lattice match with $SrTiO_3$ and the ability to single-terminate the surface. $SrRuO_3$ changes its termination on $SrTiO_3$ by first growing 1.5 unit cells of material and subsequently single unit cells. The CuO was found to grow equally well on the A site (Sr) terminated surface. $SrRuO_3$ is by no means the ideal ferromagnet with which to measure an exchange bias effect. As mentioned in section 5.1.3 on page 84, to apply the exchange bias theory it is ideal when cooling the sample in a magnetic field if the Curie temperature is higher than the Néel temperature so that all the spins in the ferromagnet are aligned first along a known direction. The antiferromagnet is then influenced by the ferromagnet when cooling down through the Néel temperature and aligns preferentially. In the case of $SrRuO_3$ the Curie temperature is only 160 K, which means the ideal scenario is only valid when the Néel temperature of CuO is below this. If the Néel temperature for the tetragonal phase is close to that of tenorite we would expect, due to the thickness effect, that measuring an exchange bias effect is possible. If the tetragonal phase has a T_N which follows the trend based on the other rock-salt structure transition metal monoxides, as was shown in figure 5.6 on page 85, we would expect T_N to be much higher than 160 K. No straightforward measurement of the exchange bias would be possible even after taking any thickness effect into account.

Due to time restraints, only two samples were measured with the Sagnac setup

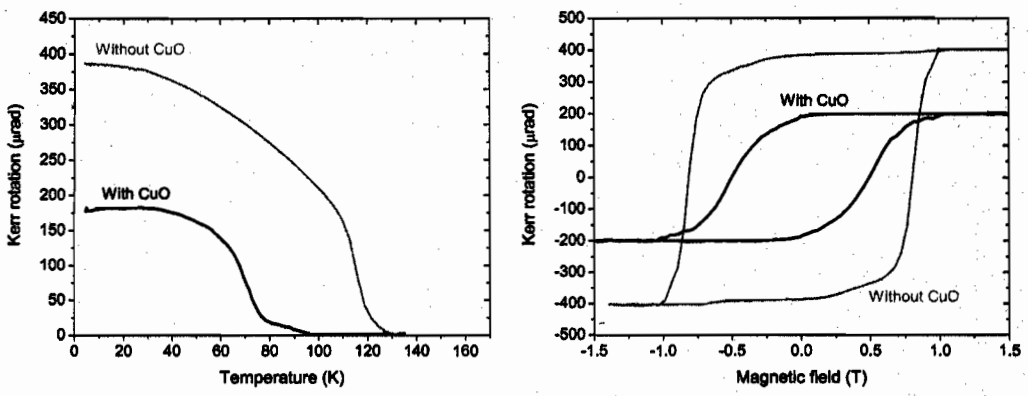

Figure 5.17: *Kerr rotation as a function of temperature on the left for 6.5 ML of $SrRuO_3$ sample, with (black lines) and without (gray lines) 300 pls CuO, which shows a reduction in the magnetic signal after the deposition of CuO. On the right the hysteresis loop taken at 4 K for the same sample. Besides a reduction in Kerr rotation the coercive field is reduced as well for part of the spins, whereas the total coercive field remains more or less the same.*

that was described in section 2.4.2 on page 23. The first had 6.5 ML of $SrRuO_3$ and the second one 9.5 ML. Both of the samples had 300 pls of CuO deposited on them. The results for the 6.5 ML sample are shown in figure 5.17, where on the left side the warm up curves for the sample with and without CuO are given. Two differences are immediately obvious: the maximum Kerr signal is much lower after CuO has been deposited (182 μrad after against 387 μrad before CuO) and the Curie temperature has been reduced as well from 130 K to 96 K. No shift in the hysteresis loop (figure 5.17 right side) and no enhancement in the coercive field are observed either. The opposite is happening, some spins are more easily flipped in the opposite direction, whereas the field that is required to flip all the spins remains unchanged.

An unexpected result was the 9.5 ML sample did not show any ferromagnetic signal after the deposition of CuO and no hysteresis loop was observed, although before deposition it showed a 650 μrad signal at 4K and a Curie temperature of 128 K.

5.3 Doping of tetragonal CuO

Doping a Mott insulator restores the electrical conductivity because empty sites are created to which electrons can jump without having to incur a cost in Coulomb energy.

If the filling of the sites or the Coulomb interaction between the sites can be controlled, the transport properties of the material can be changed. The material could be brought from an insulating to a metallic state; this is one form of a Metal-Insulator Transition, or MIT. A model with which to describe such transitions is the Hubbard model.[63,64,65] The two important parameters in the Hubbard model are the electron correlation strength U/t and the band filling n. A schematic metal-insulator phase diagram is given in figure 5.18 on the next page. The $n = 0$ and $n = 2$ fillings correspond

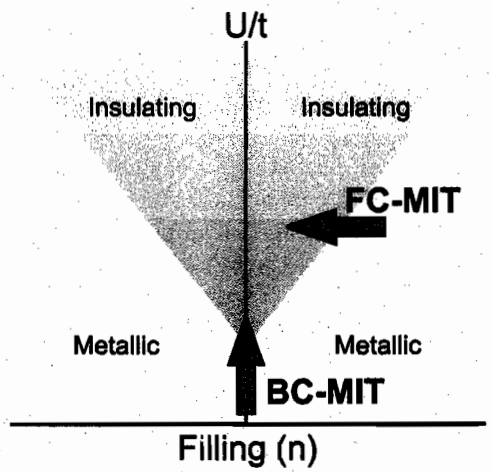

Figure 5.18: *A schematic phase diagram of a Mott insulator, taken from Imada, Fujimori, and Tokura,*[20] *showing a metal-insulator transition can be accomplished by bandwidth control (U/t) or by filling control (n). Note that this diagram is only valid when disorder plays no role.*

to the band insulator state. At half filling ($n = 1$), represented by the black line in the center of the figure, the transition from the insulating to the metallic state can be driven by changing U/t. This type of transition is called a bandwidth controlled (BC) MIT. To accomplish the transition the electron correlation strength is controlled by modifying the lattice parameters or the chemical composition while essentially maintaining the original lattice structure. The onsite (U) or intersite Coulomb interacting is kept almost unchanged during the above procedure and control of electron correlation is achieved by control of the transfer interaction (t), which is also known as the one-electron bandwidth. The one-electron bandwidth in $3d$ transition metal systems is known to be quite narrow. In the ABO_3 perovskite systems the bandwidth is reduced by the buckling B—O—B bond, since the effective $3d$-electron transfer interaction between the neighboring B sites is governed by the supertransfer process via the O $2p$ state. For CuO the $3d$-electron bandwidth is still narrow, but no buckling will occur in the rock salt structure. According to Imada, Fujimori, and Tokura[20] there are three methods of bandwidth control:

1. applying pressure to the material;
2. modifying the chemical composition using the solid solution or the mixed-crystal effect, a good example of which is the substitution of S with Se in NiS_2;
3. modifying the ionic radius of the A site in a perovskite-type compound, i.e. ABO_3.

These options are not easily accessible for our materials system, or cause us to cease measuring rock salt CuO. At the same time we need to remember that by using

epitaxy to stabilize the structure, we apply significant pressure to the material. This will influence the bandwidth of the material and might make it easier to dope, it is, however, not a parameter we can easily control. Therefore another route for doping might be more appropriate.

A filling at noninteger n usually leads to the metallic phase. The most interesting phase is the one right next to the $n = 1$ insulating line in figure 5.18 on the preceding page which is derived by filling control (FC-MIT) of the parent Mott insulator. The standard method for filling control is to replace an atom with a high valence, with one with a lower valence, or vice versa. A good example is the high-T_c compound $La_{2-x}Sr_xCuO_4$ compound where the trivalent La atoms are replaced with divalent Sr atoms. Using the insulating compound as a reference, the filling is called *hole doping* when the band filling is decreased and *electron* doping when the band filling is increased. Replacing La with Sr in $La_{2-x}Sr_xCuO_4$ is an example of hole doping. Chemical substitution is one way to accomplish different filling, but this can also be done by injecting or depleting charge carriers with an electric field or by using some kind of modulation doping.

Comparing to doping experiments in tenorite could provide good insight on where to start. However, there are few references in literature on the doping of tenorite. The most interesting experiments are those where tenorite is doped by substituting Li for Cu.[45,66] This substitution would result in hole doping, if the oxygen stoichiometry does not change. Those authors find Li only substitutes Cu up to 1.7%. With increased doping the Cu—Cu bond length is increased and the magnetic ordering temperature is decreased due to the weakening of the superexchange coupling along the $(10\bar{1})$. direction. In other related work[67] they show there is evidence for static charge ordering and alignment of charge ordered domains in CuO analogous to the charge stripes in cuprate superconductors. The fact that a simple compound like CuO shows the same electronic behavior as the high temperature superconductors is promising for doping experiments.

5.3.1 Chemical doping through charge transfer

Without breaking vacuum, alkali metals were deposited on top of the tetragonal CuO films in an attempt to transfer charge carriers into the material. The sources used are described in section 2.2.4 on page 11. Alkali metals were chosen because their outer electrons are very loosely bound and these can be transferred into the CuO. This property also makes them very reactive and that likely prevents us from analyzing the samples outside of vacuum conditions. Of course, even if charge is transferred the question remains whether the charges will be mobile or localized.

The first alkali metal used was lithium, the lightest of the alkali metals. Deposition was incremental and after each deposition photoemission spectra were taken. Valence band spectra were taken with UPS to see whether the sample was a conductor and core level spectra were taken to monitor the change in chemical environment. In figure 5.19 on the facing page the Cu $2p$ spectrum is shown as Li is being deposited. After half a monolayer of Li the spectrum changes considerably. The satellite peaks diminish in intensity whereas the main peaks gain. The spectral shift can be explained

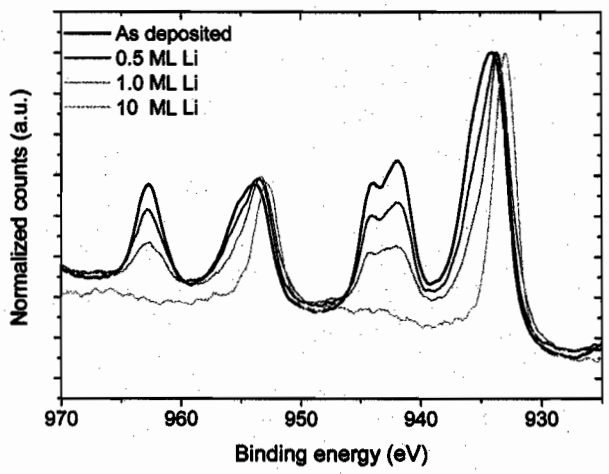

Figure 5.19: *XPS Cu 2p spectrum of an as-deposited tetragonal CuO film and spectra taken after deposition of 0.5, 1.0, and 10 MLs of Li. The spectrum changes systematically towards a Cu^{1+} spectrum, which suggests charge carriers are created.*

by doping of the Li electrons into the CuO: in a localized picture this would generate more Cu^{1+} at the expense of Cu^{2+} and make the spectrum look more like Cu_2O. On the other hand a similar effect would be expected to occur if Li removed oxygen from the CuO, which also creates more Cu^{1+}. In both cases the CuO would be electron doped, but UPS measurements showed no Fermi edge, charging was observed during XPS measurements, and when the samples were removed from the system no conductivity was measured. The RHEED spectra for the films with 0.5 and 1.0 ML of Li showed no change with respect to the as-deposited sample, whereas after 10 ML of Li the RHEED spectrum showed a disordered surface as one would expect from an amorphous layer of Li.

The Li was not easy to detect with XPS, which made it hard to verify how much had been deposited. To be better able to detect the deposited amount Li was switched for Cs. Cs has a much higher sensitivity factor for XPS and turned out to be much easier to detect. The Cu $2p$ spectra for the Cs deposition are shown in figure 5.20 on the next page and the systematic change in the spectra is similar to the sample with Li as a dopant. The O $1s$ peak does not change significantly when Cs is deposited. The Cs peaks themselves are lower than one would expect for elemental Cs by about 1 eV. CsOH is 1.4 eV lower than Cs metal and the lower binding energy therefore suggests that Cs has donated an electron. For this sample neither a Fermi edge nor conductivity outside of vacuum, after 1ML was deposited, were observed.

5.4 Discussion and conclusions

We have grown CuO with a higher degree of symmetry by using epitaxial stabilization on a $SrTiO_3$ substrate. The in-plane lattice parameters were determined by RHEED.

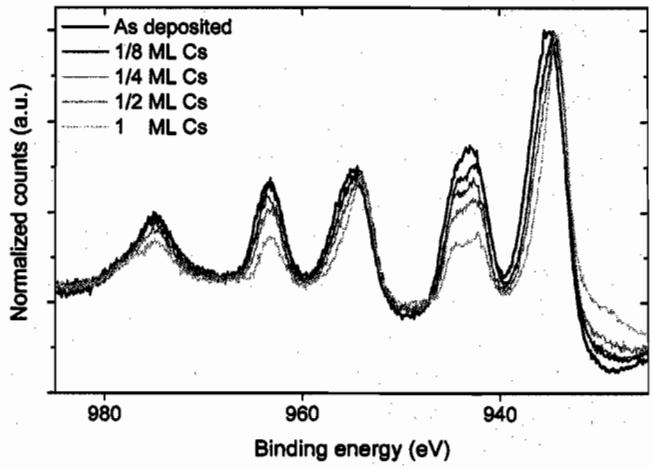

Figure 5.20: *XPS Cu 2p spectrum of an as-deposited tetragonal CuO film and spectra taken after deposition of approximately $\frac{1}{8}$, $\frac{1}{4}$, $\frac{1}{2}$, and 1.0 MLs of Cs. The spectrum changes systematically towards a Cu^{1+} spectrum, which suggests charge carriers are created.*

After taking forbidden reflections into account the CuO was found to grow cube-on-cube on the $SrTiO_3$, which results in an in-plane lattice parameter of 3.905 Å for CuO. The out-of-plane lattice parameter was measured with XPD and decided to be about 5.3 Å after comparing to simulated data. On dual terminated substrates the growth yielded a mixture of tetragonal and monoclinic CuO. The unit cell on $SrTiO_3$ is highly strained and for this reason the tetragonal CuO cannot grow coherently for more than a few nm. Using substrates with larger in-plane lattice parameters, such as $DyScO_3$ and $GdScO_3$, might be able to help relax the strain and stabilize the tetragonal structure for larger thicknesses, while at the same time influence the electron bandwidth. At the moment though there is no reliable method to single-terminate these substrates, resulting in a mixed phase growth of the CuO.

The electronic structure of the tetragonal phase of CuO was found to differ from the monoclinic phase by examining the Cu $2p$ core level structure. The main peak becomes broader and the satellite peak sharper when the tetragonal phase is formed. The intensity distribution in the satellite peak shifts more to lower binding energies. According to Van Veenendaal and Sawatsky,[34,35] the width of the main peak is related to whether the screening electrons come from the closest ligand atoms or from ligand atoms further away. This would suggest that the screening electrons are more delocalized in the tetragonal structure. Note that while the shortest Cu–O bond lengths in the tetragonal structure are similar to those in tenorite, there are also much longer bond lengths in the tetragonal structure, which might have an influence on the nature of the electrons. The structure of the satellite peak is harder to understand. The similarity with $CuCl_2$ spectra from literature is striking though.[32] Okada *et al.*[36] have performed extensive modeling of the satellite peak. They argue that the shape of the satellite peak is mostly determined by the coupling-strength ratio between the σ and

π bondings and the amount of hybridization of these states. Following their model suggests that the degree of hybridization is weaker in the tetragonal structure than in tenorite. In other words, the ionicity is stronger in the tetragonal structure.

The tetragonal structure is more stable close to the interface as is evident from angle dependent measurements. For the best samples exposure to air does not degrade the quality of the film at the interface. The tetragonal CuO is not stable under vacuum conditions over long periods of time resulting in a reduction of the films, an effect observed previously on tenorite.[24]

The UPS spectrum of tetragonal CuO is very similar to that measured for tenorite. Some notable differences include the intensity of the low energy peak, the splitting of the main peak, and a general shift of the spectrum to higher binding energies of about half an eV. Delocalized band calculations (local density approximation) performed for tenorite do not reproduce measurements. Neglecting electron correlation effects results in an incomplete DOS spectrum and a conducting ground state. The best predictions come from cluster calculations (configuration interaction (CI) calculations), which predict the entire spectrum accurately, but shifted to slightly lower binding energy. Eskes *et al.*[62] have investigated the nature of the first ionization state of CuO, which has either a triplet or a singlet character. The singlet state peak is the one closest to the Fermi level (1.9 eV in our spectrum) and the triplet state is the next one up (3.6 eV for this work). The energy difference between these peaks is closely related to the Cu–O distances, specifically the ratio between the Cu–O distance out-of-plane and in-plane, which is about 1.4 for the tetragonal unit cell. Based on their model we would expect to see an energy difference of 0.85 eV between the two peaks. The measured distance is much larger for reasons that are not well understood.

The magnetic properties were studied by measuring the exchange bias effect on a very limited number of samples with an interface of CuO and $SrRuO_3$. Instead of increased coercivity and a shifted hysteresis loop, we observed a decrease in coercivity for part of the spins, no shift in the hysteresis loop, and a reduction in Kerr signal in general after deposition of the CuO. Thus far, no explanation has been found for these behaviors and more samples should be measured before any conclusions can be drawn.

We have attempted to dope the CuO by depositing alkali metals on top, which might donate an electron to the CuO. Li and Cs were tried and showed similar results. In both cases the Cu $2p$ XPS spectrum changed from Cu^{2+} to Cu^{1+}, suggesting either a direct doping of electrons by the alkali metal or oxygen reduction in the CuO due to the metal. In both cases the CuO would be electron doped.

Bibliography

1. E. V. Parini, V. G. Tsirel'son, and R. P. Ozerov, Soviet Physics Crystallography **33**, 175 (1988).

2. A. Kirfel and K. Eichhorn, Acta Crystallographica A **46**, 271 (1990).

3. S. Åsbrink and L.-J. Norrby, Acta Crystallographica Section B **26**, 8 (1970).

4. N. Datta and J. W. Jeffery, Acta Crystallographica B **34**, 22 (1978).

5. M. O'Keeffe and J.-O. Bovin, American Mineralogist **63**, 180 (1978).

6. P. E. D. Morgan, D. E. Partin, B. L. Chamberland, and M. O'Keeffe, Journal of Solid State Chemistry **121**, 33 (1996).

7. J. R. Schrieffer and J. S. Brooks, eds., *Handbook of High Temperature Superconductivity: Theory and Experiment* (Springer, 2007).

8. F. A. Cotton and G. Wilkinson, *Advanced Inorganic Chemistry* (Wiley Interscience, 1988), 5th ed.

9. J. F. Pierson, A. Thobor-Keck, and A. Billard, Applied Surface Science **210**, 359 (2003).

10. L. Kleinman and K. Mednick, Physical Review B **21**, 1549 (1980).

11. J. Robertson, Physical Review B **28**, 3378 (1983).

12. E. Ruiz, S. Alvarez, P. Alemany, and R. A. Evarestov, Physical Review B **56**, 7189 (1997).

13. Y. L. Liu, Y. C. Liu, R. Mu, H. Yang, C. L. Shao, J. Y. Zhang, Y. M. Lu, D. Z. Shen, and X. W. Fan, Semiconductor Science and Technology **20**, 44 (2005).

14. Z. Szotek, W. M. Temmerman, and H. Winter, Physical Review B **47**, 4029 (1993).

15. F. Marabelli, G. B. Parravicini, and F. Salghetti-Drioli, Physical Review B **52**, 1433 (1995).

16. F. P. Koffyberg and F. A. Benko, Journal of Applied Physics **53**, 1173 (1982).

17. N. Ashcroft and N. Mermin, *Solid State Physics* (Harcourt, 1976).

18. N. F. Mott, Proceedings of the Royal Society of London Series A **62**, 416 (1949).

19. J. Orenstein and A. Millis, Science **288**, 468 (2000).

20. M. Imada, A. Fujimori, and Y. Tokura, Reviews of Modern Physics **70**, 1039 (1998).

21. S. Huefner, Solid State Communications **49**, 1177 (1984).

22. J. Zaanen, G. A. Sawatzky, and J. W. Allen, Physical Review Letters **55**, 418 (1985).

23. J. Ghijsen, L. H. Tjeng, J. van Elp, H. Eskes, J. Westerink, G. A. Sawatzky, and M. T. Czyzyk, Physical Review B **38**, 11322 (1988).

24. Z.-X. Shen, R. S. List, D. S. Dessau, F. Parmigiani, A. J. Arko, R. Bartlett, B. O. Wells, I. Lindau, and W. E. Spicer, Physical Review B **42**, 8081 (1990).

25. K. Hirokawa, F. Honda, and M. Oku, Journal of Electron Spectroscopy and Related Phenomena **6**, 333 (1975).

26. J. C. Fuggle and N. Mårtensson, Journal of Electron Spectroscopy and Related Phenomena **21**, 275 (1980).

27. N. Nücker, J. Fink, B. Renker, D. Ewert, C. Politis, P. J. W. Weijs, and J. C. Fuggle, Zeitschrift für Physik B **67**, 9 (1987).

28. N. S. McIntyre and M. G. Cook, Analytical Chemistry **47**, 2208 (1975).

29. T. H. Fleisch, G. W. Zajac, J. O. Schreiner, and G. J. Mains, Applied Surface Science **26**, 488 (1986).

30. T. Robert, M. Bartel, and G. Offergeld, Surface Science **33**, 123 (1972).

31. E. Antonides, E. C. Janse, and G. A. Sawatzky, Physical Review B **15**, 1669 (1977).

32. G. van der Laan, C. Westra, C. Haas, and G. A. Sawatzky, Physical Review B **23**, 4369 (1981).

33. S. Hüfner, G. K. Wertheim, and J. H. Wernick, Solid State Communications **17**, 417 (1975).

34. M. A. van Veenendaal and G. A. Sawatzky, Physical Review Letters **70**, 2459 (1993).

35. M. A. van Veenendaal, H. Eskes, and G. A. Sawatzky, Physical Review B **47**, 11462 (1993).

36. K. Okada and A. Kotani, Journal of the Physical Society of Japan **58**, 2578 (1989).

37. T. Saitoh, A. E. Bocquet, T. Mizokawa, and A. Fujimori, Physical Review B **52**, 7934 (1995).

38. P. W. Anderson, Physical Review **115**, 2 (1959).

39. W. A. Harrison, Physical Review B **76**, 054417 (2007).

40. D. Alders, L. H. Tjeng, F. C. Voogt, T. Hibma, G. A. Sawatzky, C. T. Chen, J. Vogel, M. Sacchi, and S. Iacobucci, Physical Review B **57**, 11623 (1998).

41. J. A. Borchers, M. J. Carey, R. W. Erwin, C. F. Majkrzak, and A. E. Berkowitz, Physical Review Letters **70**, 1878 (1993).

42. R. W. Wang and D. L. Mills, Physical Review B **46**, 11681 (1992).

43. T. Ambrose and C. L. Chien, Physical Review Letters **76**, 1743 (1996).

44. A. S. Carriço and R. E. Camley, Physical Review B **45**, 13117 (1992).

45. K. Saito, S. Ikeuchi, Y. Nakazawa, X. G. Zheng, M. B. Maple, and M. Sorai, Solid State Communications **125**, 23 (2003).

46. W. L. Roth, Physical Review **111**, 772 (1958).

47. J. Stöhr, A. Scholl, T. J. Regan, S. Anders, J. Lüning, M. R. Scheinfein, H. A. Padmore, and R. L. White, Physical Review Letters **83**, 1862 (1999).

48. W. H. Meiklejohn and C. P. Bean, Physical Review **102**, 1413 (1956).

49. R. L. Stamps, Journal of Physics D: Applied Physics **33**, R247 (2000).

50. A. Scholl, J. Stöhr, J. Lüning, J.-P. Locquet, J. Fompeyrine, J. W. Seo, H. Siegwart, F. Nolting, S. Anders, E. Fullerton, et al., Science **287**, 1014 (2000).

51. J. van Driel, F. R. de Boer, K.-M. H. Lenssen, and R. Coehoorn, Journal of Applied Physics **88**, 975 (2000).

52. H. Xi and R. M. White, Physical Review B **61**, 80 (2000).

53. F. Nolting, A. Scholl, J. Stohr, J. Seo, J. Fompeyrine, H. Siegwart, J.-P. Locquet, S. Anders, J. Luning, E. Fullerton, et al., Nature **405**, 767 (2000).

54. D. Mauri, H. C. Siegmann, P. S. Bagus, and E. Kay, Journal of Applied Physics **62**, 3047 (1987).

55. X. Y. Lang, W. T. Zheng, and Q. Jiang, Nanotechnology **18**, 155701 (2007).

56. F. J. García de Abajo, M. A. Van Hove, and C. S. Fadley, Physical Review B **63**, 075404 (2001).

57. C. J. Powell and A. Jablonski, *NIST Electron Inelastic-Mean-Free-Path Database* (National Institute of Standards and Technology, Gaithersburg, MD, 2000), 1st ed.

58. W. Y. Ching, Y.-N. Xu, and K. W. Wong, Physical Review B **40**, 7684 (1989).

59. J. Ghijsen, L. H. Tjeng, H. Eskes, G. A. Sawatzky, and R. L. Johnson, Physical Review B **42**, 2268 (1990).

60. S. Warren, W. R. Flavell, A. G. Thomas, J. Hollingworth, P. L. Wincott, A. F. Prime, S. Downes, and C. Chen, Journal of Physics: Condensed Matter **11**, 5021 (1999).

61. M. Takahashi and J.-I. Igarashi, Physical Review B **56**, 12818 (1997).

62. H. Eskes, L. H. Tjeng, and G. A. Sawatzky, Physical Review B **41**, 288 (1990).

63. J. Hubbard, Proceedings of the Royal Society of London Series A **276**, 238 (1963).

64. J. Hubbard, Proceedings of the Royal Society of London Series A **277**, 237 (1964).

65. J. Hubbard, Proceedings of the Royal Society of London Series A **281**, 401 (1964).

66. X. G. Zheng, H. Yamada, D. J. Scanderbeg, M. B. Maple, and C. N. Xu, Physical Review B **67**, 214516 (2003).

67. X. G. Zheng, C. N. Xu, E. Tanaka, Y. Tomokiyo, H. Yamada, Y. Soejima, Y. Yamamura, and T. Tsuji, Journal of the Physical Society of Japan **70**, 1054 (2001).